Advances in Radiation Oncology (2024) 9, 101271

advances in radiation oncology

www.advancesradonc.org

Scientific Article

Association of Internal and External Motion Based on Cine MR Images Acquired During Real-Time Treatment on MRI–Guided Linear Accelerator for Patients With Lung Cancer

Weihua Mao, PhD,* Joshua Kim, PhD, and Indrin J. Chetty, PhD

Department of Radiation Oncology, Henry Ford Cancer Institute, Detroit, Michigan

Received 15 August 2022; accepted 8 May 2023

Purpose: With the recent clinical implementation of magnetic resonance imaging (MRI)-guided linear accelerators, a large number of real-time planar MR images has been acquired during lung cancer treatment as a standard of care. In this study, associations among lung tumor, diaphragm, and external skin movement were studied based on MR cine imaging during the entire duration of each treatment fraction.

Methods and Materials: This retrospective study used 181,798 planar MRI frames acquired over 55 treatment/imaging sessions of 13 patients with lung cancer treated on 2 MRI-guided linear accelerators. From each planar MR image frame, in-house software automatically extracted 9 features: the superior-interior (SI) and posterior-anterior (PA) positions of a lung tumor; the area of the lung (Lung_Area); the posterior (Dia_Post), dome/apex (Dia_Dome), and anterior (Dia_Ant) points of a diaphragmatic curve; the diaphragm curve point (Dia_Max); and the chest (Chest) and belly (Belly) skin points experienced the maximum range of motions. Correlation analyses were performed among the 9 features for every session. Lung tumor motion range and standard deviations were calculated based on positions obtained in cine images and compared with motion ranges obtained from 4-dimensional computed tomography images.

Results: In the study, 177,009 frames of images were successfully analyzed. For all patients, correlation coefficients were as follows: 0.91 $\pm$ 0.10 between any 2 features among Lung_Area, Dia_Post, Dia_Dome, and Dia_Max; 0.82 $\pm$ 0.21 between SI and any feature among Lung_Area, Dia_Post, Dia_Dome, and Dia_Max; 0.75 $\pm$ 0.24 between SI and Belly. Six of 13 patients were considered large amplitude motion (patients with lung tumor SI motion standard deviation >5 mm). Furthermore, 92,956 frames of images were analyzed for the 6 large-amplitude motion patients. For this set, correlation coefficients were 0.93 $\pm$ 0.07 between any 2 features among Lung_Area, Dia_Post, Dia_Dome, and Dia_Max; 0.94 $\pm$ 0.06 between SI and any feature among Lung_Area, Dia_Post, Dia_Dome, and Dia_Max; and 0.90 $\pm$ 0.09 between SI and Belly.

Conclusions: Both belly and diaphragmatic motions as assessed by cine MRI are highly correlated with large amplitude lung tumor motion in the longitudinal axis.

Introduction

Internal tumor and organ motion due to respiration compromises the efficacy of radiation therapy at

Sources of support: This work had no specific funding.

The data that support the findings of this study are available from the corresponding author upon reasonable request.

Corresponding author: Weihua Mao, PhD; E-mail: weihuamao@gmail.com

https://doi.org/10.1016/j.adro.2023.101271

delivering high radiation doses to the tumor while sparing adjacent normal tissues. As a result, large planning margins have been added to expand a target to a much larger planning treatment volume.[1-3] It is essential to locate tumors and critical structures during treatment to minimize planning margins.[4-7] X-ray based fluoroscopy imaging can monitor internal motion but imaging dose can be excessive.[8] Implanted anchored beacons can track real-time locations of points within the tumor; however, there is risk of side effects from fiducial implantation and marker migration.[9,10] Correlation between internal tumor motion and external surrogates has been studied based on patient data, such as acquisition of periodic computed tomography (CT) or magnetic resonance (MR) volumetric image sets, which are sometimes dynamically updated with intermittent x-ray or MR images during treatment.[11-24] For instance, Paganelli et al used 120 frames of MR cine images over 74.4 seconds per patient[25]; Yang et al studied MR imaging (MRI) within 15 to 30 second intervals.[26] However, respiratory patterns may be different during treatment from the patterns acquired at simulation and can even change within a treatment session. Therefore, understanding of the motion correlations during a period long enough for an entire treatment fraction may be clinically relevant. Since the recent clinical implementation of MR-guided linear accelerators (LINACs), an enormous amount of continuous planar MRI data has been acquired in real-time as part of routine radiation therapy treatment.[5-7] Liver tumor motion has been recently studied based on large amounts of MR cine data acquired during real-time treatment.[27] Strong correlations were found between liver tumor and diaphragm and the correlation between liver tumor and belly movement was found to be affected by changes in respiratory patterns. In this report, the associations between lung tumor/diaphragm and external surface/skin were studied using a vast quantity of MR cine images acquired during lung cancer treatment.

Methods and Materials

Patient cine images routinely acquired during treatments on 2 low field (0.35 T) MRI LINACs (MRIdian; ViewRay, Denver, CO) were used for this institutional review board—approved (IRB# 12934) retrospective study. The MRI LINACs continuously acquire 4 frames of sagittal MR images per second during treatment as part of the treatment monitoring process. Each image frame has dimensions of 100 × 100 pixels (3.5 × 3.5 mm). A target tracking structure is contoured on the volumetric image and then deformably propagated onto each image frame by the treatment software. Similarly, the treatment software generates a boundary structure by expanding the original target structure by 3 mm isotropically and rigidly propagating it onto each newly acquired image frame. As shown in Fig. 1A, the target (red contour) and boundary (yellow contour) contours were overlaid on grayscale planar MR images. The treatment software saves cine images with contours, which were exported as videos for each treatment session. The image dimensions of the saved cine images changed after a software upgrade in the middle of the period when enrolled patients were treated. For the original software (V0), videos were exported with dimensions of 944 × 944 pixels (0.37 × 0.37 mm), and for the upgraded version (V2), videos were exported with dimensions of 512 × 512 pixels (0.79 × 0.79 mm). MR images were analyzed automatically using in-house-developed MATLAB (The MathWorks, Natick, MA) scripts.[27] After target and boundary contours were detected on grayscale images based on color indices, they were removed and filled by average intensities of surrounding pixels (Fig. 1B). Target contours were filled separately to calculate target position, target contour center-of-mass in the posterior-anterior (PA) and superior-inferior (SI) directions. Body and lung structures (Fig. 1C) were detected separately by different intensity thresholds after image processing with MATLAB internal functions

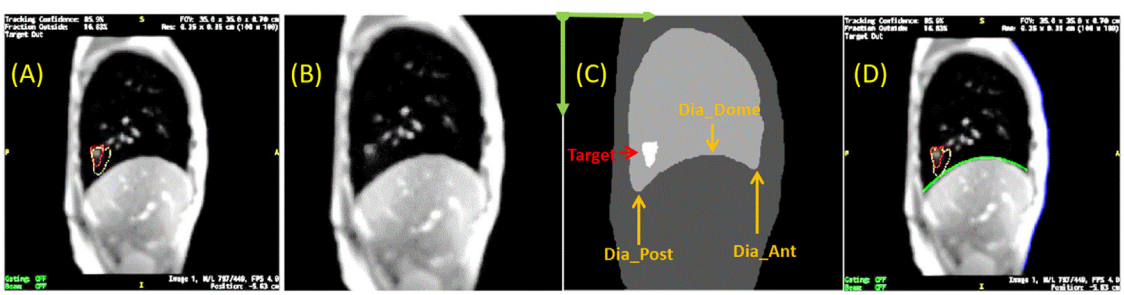

Figure 1 Sample of magnetic resonance image analysis. (A) Acquired image with target (red) and boundary (yellow) contours overlaid. (B) Cropped image after contours were removed. (C) Detected body, lung, and target contours superimposed. Dia_Dome, Dia_Post, Dia_Ant, and Target are labeled. The origin of the coordinate system is located in the upper-left corner. Axis directions are indicated by green arrows. (D) Detected body (in blue color) and diaphragmatic curve (in green color) superimposed back onto the original image.

including imdilate, imfill, and imerode. The diaphragmatic curves were extracted from the inferior aspect of the lung. The diaphragmatic curves were fitted using parabolic functions. The most posterior point (Dia_Post) and the most anterior point (Dia_Ant) on the patient diaphragmatic curve were extracted, which represented the choice of starting and ending points. A leveled rectangle with the smallest size was determined to enclose the diaphragmatic curve. If the superior-inferior height of the rectangle was smaller than half of its posterior-anterior width, full diaphragmatic curve was used for curve-fitting. Otherwise, only the upper quarter portion of the diaphragmatic curve was used for curve-fitting as demonstrated in Fig. E1.

Six features were automatically detected on every image frame: target position (PA and SI); the area of the lung (Lung_Area); and 3 diaphragmatic curve points, Dia_Post, Dia_Ant, and the dome or apex (Dia_Dome) of the curve-fitted parabolic curves, as illustrated in Fig. 1C.[28]

Three additional features were determined based on motion ranges over each treatment session. Motion ranges were computed for every point on the diaphragmatic curve, chest region, and belly region. Three points were selected: the point on the diaphragm curve that experienced the maximum range of longitudinal motion over the treatment session (Dia_Max) and the chest skin point (Chest) and belly skin point (Belly) that experienced the maximum range of motion in the anterior/posterior direction.

A preanalysis screening process was performed automatically before correlation analysis. Histograms were analyzed with a bin width of 3.5 mm for target SI and PA positions and Belly positions for each session. For each histogram, the last bin with <1% relative occurrence from the most frequent position to the maximum position was defined as high end cutoff point. The first bin with <1% relative occurrence from the most frequent position to the minimum position was defined as the low-end cutoff point. Any points beyond the low-end and high-end cutoffs were considered extreme positions. Image frames with extreme positions were excluded from correlation analysis. These motions were likely due to occasional, sudden large target excursions, where the target was not properly detected. Pearson correlation analyses were performed for each pair of features among the 9 aforementioned features for every session resulting in 36 corresponding correlation coefficients.

A total of 13 patients with lung cancer (Table 1) treated on either of 2 MRI-guided LINACs were enrolled in this study. Patients were prescribed to 48 Gy in 4 fractions, 40 Gy in 4 fractions, 40 Gy in 5 fractions, 50 Gy in 5 fractions, or 54 Gy in 3 fractions. When one treatment fraction was interrupted and resumed after repositioning, multiple sessions were recorded for one planned fraction of treatment. In total, 181,798 frames of MR sagittal images were acquired in this study.

Four-dimensional (4D) CT scans were acquired during treatment simulation for 10 patients. Each 4D CT image set contained 10 phases of images based on phase sorting. Lung tumor motion ranges in the 3 cardinal dimensions were obtained for each phase using in-house-developed MATLAB scripts. The superior-inferior motion (peak-peak) ranges are listed in Table 1.

Table 1 List of patients with PTV size and treatment prescriptions

Patients	Sex	Age (y)	Tumor location	PTV (cm^3)	Prescription
LN01	F	82	Right upper lobe	21.4	12 Gy × 4
LN02	F	82	Right middle lobe	24.5	12 Gy × 4
LN03	M	70	Right middle lobe	10.6	12 Gy × 4
LN04	M	62	Right middle lobe	12.6	12 Gy × 4
LN05	F	76	Right upper lobe	10.8	12 Gy × 4
LN06	M	70	Left lower lobe	21.2	8 Gy × 5
LN07	F	66	Right hilum	13.8	12 Gy × 4
LN08	F	50	Left lower lobe	19.4	12 Gy × 4
LN09	M	71	Right middle lobe	13.6	10 Gy × 4
LN10	F	69	Right lower lobe	10.3	12 Gy × 4
LN11	F	74	Right middle lobe	13.6	10 Gy × 4
LN12	M	50	Left upper lobe	17.4	18 Gy × 3
LN13	M	76	Right lower lobe	82.1	10 Gy × 5

Abbreviations: F = female; M = male; PTV = planning target volume.

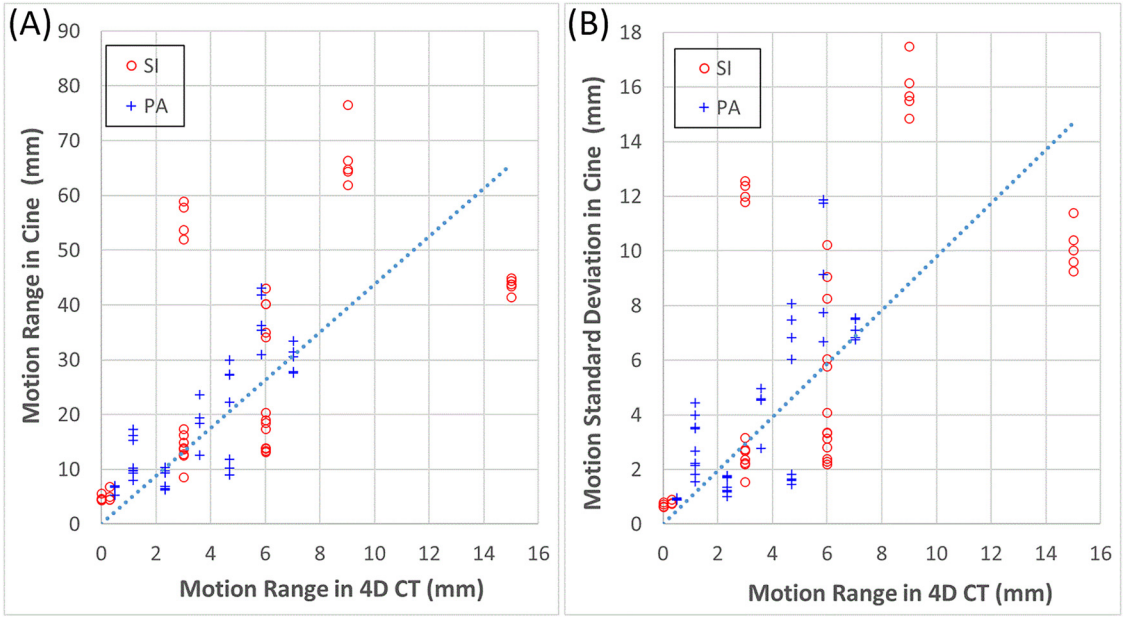

Figure 2 Comparison of target motion range (A) and standard deviation (B) of SI and PA in cine images against motion in 4D CT. Linear curve fitting is displayed for SI motions only. *Abbreviations*: 4D CT = 4-dimensional computed tomography; PA = posterior-anterior; SI = superior-interior.

Results

In the study, 177,009 frames of 2-dimensional MR images were analyzed in 55 imaging sessions for 13 patients. Approximately 2.6% of images were excluded mainly due to the target not being detected by the system. Figure 2 compares PA and SI target motion ranges and standard deviations against corresponding motion ranges obtained with 4D CT. The ratio between target SI motion standard deviation in cine images and SI motion range in 4D CT was 0.98 (Fig. 2B). Using a motion standard deviation threshold of 5 mm, based on cine MRI data, 7 patients had minor SI motions. The remaining 6 patients with 92,956 frame images were regarded as patients with large amplitude tumor motions. Table 2 summarizes correlation coefficients of 36 feature pairs among the 9 features defined previously. The correlation coefficient results for all patients and large-amplitude motion patients are listed in the right top half and left lower half list of the table, respectively. For all patients, correlation coefficients were as follows: 0.91 ± 0.10 for all 6 pairs of features among Dia_Post, Dia_Dome, Dia_Max, and Lung_Area; 0.82 ± 0.21 for 4 pairs of features between SI and any of Dia_Post, Dia_Dome, Dia_Max, and Lung_Area; and 0.75 ± 0.24 between SI and Belly. For the 6 large-motion patients with 28 sessions, aggregate correlation coefficients were 0.93 ± 0.07 over all combinations of 2 features among Dia_Post, Dia_Dome, Dia_Max, and Lung_Area; 0.94 ± 0.06 over all combinations of SI and any feature among Dia_Post, Dia_Dome, Dia_Max, and Lung_Area; and 0.90 ± 0.09 between SI and Belly.

Negative correlation coefficients were observed for 1 patient: LN05, −0.83 ± 0.05 (range, −0.87 to −0.77). Detailed studies found expansion of lung after inhalation leads to the upper lobe tumor moving up and diaphragm moving down. Absolute values of correlation coefficients were used for statistical analysis. Figure 3 shows the absolute SI-Belly correlation coefficients as a function of motion range (cine imaging motion standard deviations).

Results for all 55 session results were visually reviewed. Patient LN09 showed hysteresis (Fig. 4), defined as the presence of more than 1 y-axis position for each position on the x-axis. For instance, in Fig. 4A, which shows PA versus SI motion (session 1 of patient LN09), there are clearly more than 1 SI position for each PA position, which defines the hysteresis. Such hysteresis was not observed for the other 12 of 13 patients.

Discussion

It was expected that motion ranges obtained from 4D CT would be different from those observed from the cine treatment images because 4D CT reconstruction tends to smear out extreme/irregular motions at end of inhale or exhale.[29,30] Figure 2 indicates that the cine image motion standard deviation is similar to the motion peak-peak range obtained from 4D CT. Other studies have demonstrated deviation between motion standard deviations observed of a tumor surrogate and that from 4D CT peak-to-peak motion. For instance, Steiner et al[30] reported significant variation between motion standard

Table 2 Correlation coefficients between pairs of the 9 parameters

All / Large	PA	SI	Dia_Post	Dia_Dome	Dia_Ant	Lung_Area	Dia_Max	Chest	Belly
PA		0.62 ± 0.27 [0.03, 0.96]	0.60 ± 0.29 [0.06, 0.93]	0.72 ± 0.26 [0.05, 0.97]	0.71 ± 0.29 [0.01, 0.97]	0.72 ± 0.27 [0.06, 0.97]	0.66 ± 0.24 [0.09, 0.95]	0.69 ± 0.22 [0.04, 0.97]	0.67 ± 0.26 [0.01, 0.96]
SI	0.75 ± 0.20 [0.36, 0.96]		0.81 ± 0.23 [0.09, 0.99]	0.83 ± 0.19 [0.23, 0.99]	0.72 ± 0.27 [0.01, 0.98]	0.83 ± 0.20 [0.03, 0.98]	0.82 ± 0.22 [0.09, 0.99]	0.60 ± 0.25 [0.02, 0.93]	0.75 ± 0.24 [0.10, 0.99]
Dia_Post	0.73 ± 0.26 [0.06, 0.93]	0.94 ± 0.08 [0.62, 0.99]		0.89 ± 0.11 [0.52, 0.99]	0.68 ± 0.26 [0.09, 0.99]	0.92 ± 0.08 [0.54, 0.99]	0.89 ± 0.15 [0.44, 1.00]	0.68 ± 0.16 [0.34, 0.93]	0.80 ± 0.17 [0.26, 0.99]
Dia_Dome	0.87 ± 0.10 [0.58, 0.97]	0.94 ± 0.07 [0.70, 0.99]	0.91 ± 0.08 [0.72, 0.99]		0.85 ± 0.21 [0.18, 0.99]	0.94 ± 0.07 [0.56, 0.99]	0.91 ± 0.08 [0.73, 1.00]	0.68 ± 0.19 [0.09, 0.97]	0.80 ± 0.19 [0.13, 0.99]
Dia_Ant	0.86 ± 0.11 [0.39, 0.97]	0.79 ± 0.22 [0.25, 0.98]	0.76 ± 0.22 [0.27, 0.99]	0.92 ± 0.13 [0.35, 0.99]		0.79 ± 0.23 [0.06, 0.99]	0.73 ± 0.24 [0.18, 0.99]	0.57 ± 0.26 [0.10, 0.96]	0.68 ± 0.26 [0.05, 0.98]
Lung_Area	0.87 ± 0.11 [0.57, 0.97]	0.93 ± 0.04 [0.76, 0.98]	0.93 ± 0.06 [0.76, 0.98]	0.97 ± 0.01 [0.94, 0.99]	0.87 ± 0.16 [0.34, 0.99]		0.92 ± 0.08 [0.61, 0.99]	0.79 ± 0.14 [0.40, 0.96]	0.84 ± 0.14 [0.37, 0.97]
Dia_Max	0.77 ± 0.16 [0.35, 0.95]	0.95 ± 0.06 [0.79, 0.99]	0.90 ± 0.11 [0.66, 1.00]	0.91 ± 0.07 [0.76, 1.00]	0.77± 0.22 [0.28, 0.98]	0.93 ± 0.05 [0.76, 0.98]		0.69 ± 0.19 [0.18, 0.92]	0.78 ± 0.17 [0.39, 0.98]
Chest	0.78 ± 0.14 [0.39, 0.94]	0.69 ± 0.21 [0.23, 0.93]	0.71 ± 0.17 [0.42, 0.93]	0.75 ± 0.18 [0.43, 0.97]	0.68 ± 0.23 [0.24, 0.96]	0.84 ± 0.13 [0.55, 0.96]	0.72 ± 0.18 [0.34, 0.92]		0.76 ± 0.21 [0.17, 0.99]
Belly	0.80 ± 0.13 [0.36, 0.95	0.90 ± 0.09 [0.64, 0.99]	0.88 ± 0.10 [0.65, 0.99]	0.92 ± 0.07 [0.68, 0.99]	0.81 ± 0.19 [0.28, 0.98]	0.92 ± 0.07 [0.68, 0.97]	0.88 ± 0.13 [0.53, 0.98]	0.76 ± 0.21 [0.27, 0.98]	

Abbreviations: Belly = belly skin point; Chest = chest skin point; Dia_Ant = anterior point of a diaphragmatic curve; Dia_Dome = dome/apex point of a diaphragmatic curve; Dia_Max = diaphragm curve point; Dia_Post = posterior point of a diaphragmatic curve; Lung_Area = area of the lung; PA = posterior-anterior; SI = superior-interior.

Separated by the diagonal line, the right-upper half and left-lower half are correlation coefficients for full motion and high amplitude motion results, respectively. Every cell lists the average ± standard deviation and [minimum, maximum] of correlation coefficients over 55 imaging sessions. Key correlation coefficient results are highlighted in different colors. Correlation coefficients of all feature pairs among Dia_Post, Dia_Dome, Dia_Max, and Lung_Area are highlighted in green; correlation coefficients between SI and any among Dia_Post, Dia_Dome, Dia_Max, and Lung_Area are highlighted in blue; and correlation coefficients between Belly and PA or SI are highlighted in orange.

deviation measured using electromagnetic transponder surrogates (Calypso) and 4D CT peak-peak motion range: the ratio between the 2 was 0.4. One reason the motion standard deviation is larger in this study is that 12 of 13 patients were asked to hold their breath at the end of inhale or exhale for treatment while 4D CT scans were acquired at free breathing. Since 4D CT motion range is clinically accessible in most institutions, we use cine image motion standard deviation to assess motion in this study.

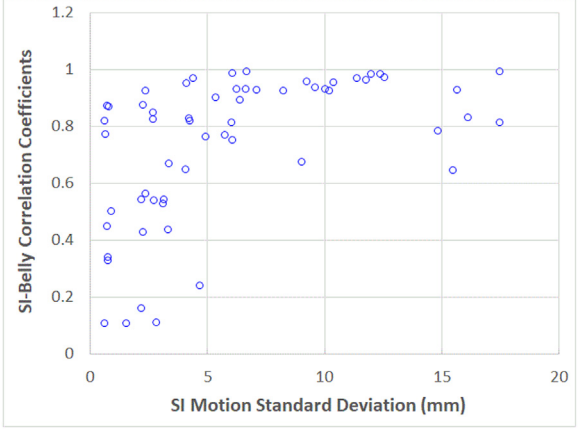

Figure 3 SI-Belly correlation coefficient as functions of SI motion standard deviation. *Abbreviation*: SI = superior-interior.

Internal-external motion correlation is not stable for minor motion as shown in Fig. 3. As a reference, during clinical motion range assessment based on 4D CT images at our institution, motion peak-peak range of 1 cm is typically used as a threshold for large-amplitude motion. In this study we considered motion standard deviations <5 mm as small-amplitude motion. Based on these criteria we found that internal/external motion correlations are not definitive for minor lung tumor motions. Six patients were considered large-amplitude motion patients. They had SI-Belly correlation coefficients of 0.90 ± 0.09 compared with the corresponding 0.75 ± 0.24 for all patients. The SI-Dia_Dome correlation coefficients were 0.94 ± 0.07 compared with 0.83 ± 0.19 for all patients. The Dia_Dome-Belly correlation coefficients were 0.92 ± 0.07 compared with 0.80 ± 0.19 for all patients.

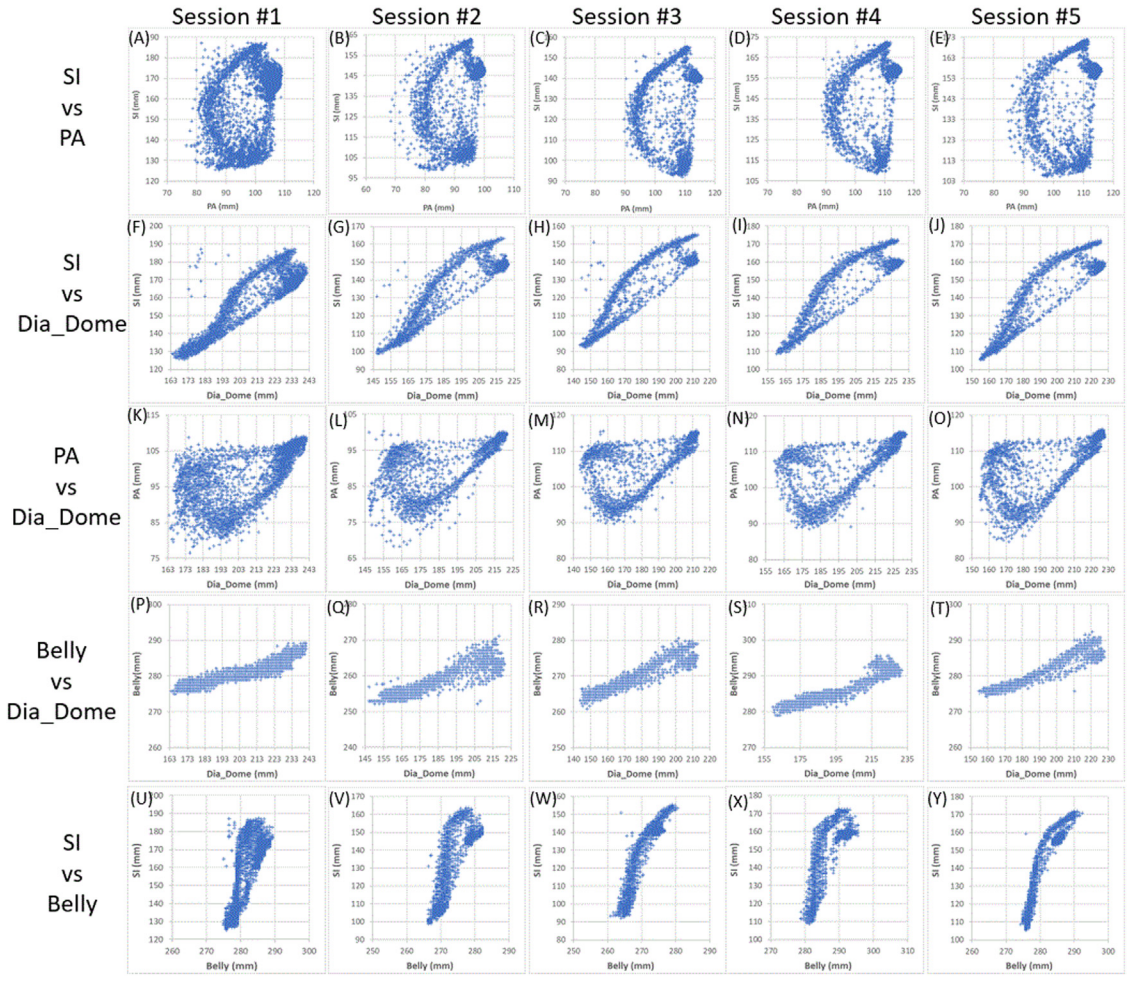

Figure 4 Dependence between features for 5 sessions of patient LN09. (A-E) SI as a function of PA in 5 sessions. (F-J) SI as a function of Dia_Dome in 5 sessions. (K-O) PA as a function of Dia_Dome in 5 sessions. (P-T) Belly as a function of Dia_Dome in 5 sessions. (U-Y) SI as a function of Belly in 5 sessions. *Abbreviations*: PA = posterior-anterior; SI = superior-interior.

Five lung/diaphragmatic features were extracted on every image frame and analyzed. Among these features, aggregate cross correlations between any 2 features among Dia_Post, Dia_Dome, Dia_Max, and Lung Area, as highlighted in green in Table 2, were 0.91 ± 0.10 and 0.93 ± 0.07 for all patients and large-amplitude motion patients, respectively. Similar to the liver patient study,[27] the feature, Dia_Ant, did not have high aggregate correlations with other features. They were 0.76 ± 0.24 and 0.83 ± 0.19 for all patients and large-motion patients, respectively. Dia_Ant detection might be susceptible when the image intensity in that region is not clear, and therefore, the identified Dia_Ant position would not be a good indicator of the anterior position or diaphragm motion. The other 4 features had similar correlations with SI while Dia_Dome and Lung_Area showed much better correlation with PA than Dia_Post or Dia_Max. The superior regions of lungs may sometimes be outside of the field of view. Therefore, the Lung_Area parameter may not represent the full lung area, and this may degrade the accuracy of the correlation between Lung_Area and other features. Dia_Dome was the most reliable landmark to represent diaphragmatic motion, which is consistent with findings reported by Yang et al.[26]

Typically, upper abdominal surface points are monitored as external surrogates of respiratory motion. For example, the Varian Real-time Position Management block or Philips Bellows is placed at the skin region experiencing maximum motion. We are searching for the skin point with the maximum motion range to simulate the most optimal external surrogate. Chest has lower correlation coefficients in aggregate than any other feature. Good correlation between Chest and PA was expected for pure chest breathing. However, correlation coefficients between Chest and PA were 0.70 ± 0.22 and 0.77 ± 0.14 for all patients and large-motion patients, respectively. Correlation coefficients between Chest and SI were only 0.60 ± 0.25 and 0.69 ± 0.21 for all patients and large-

motion patients, respectively. One reason for the weak correlation is possibly that Chest experienced the smallest range of motion among the 9 features investigated. Motion standard deviations were 3.1 ± 1.3 mm, 3.4 ± 1.2 mm, and 3.9 ± 2.7 mm for Chest, Belly, and PA, respectively. Such small motion ranges may result in large uncertainties relative to the pixel size (3.5 mm) of the original MR images. Belly motion showed much stronger correlation with both diaphragmatic and target motions than Chest motion. Correlation coefficients between Belly and Dia_Dome are 0.83 ± 0.19 and 0.94 ± 0.07 for all patients and large-motion patients, respectively. Among the patients with large motions, only 1 patient, LN09, had larger Chest motions (4.8 ± 0.3 mm) than Belly motions (4.0 ± 0.4 mm). However, this patient had higher SI-Belly correlation coefficients (0.80 ± 0.10) than SI-Chest correlation coefficients (0.77 ± 0.07). For all patients, Chest had slightly stronger correlation with PA (0.69 ± 0.22) than Belly (0.67 ± 0.26), but for patients with large-amplitude motions, PA-Chest correlation coefficients were 0.78 ± 0.14 and PA-Belly correlation coefficients are 0.80 ± 0.13. This suggests that generally Belly is a better surrogate of tumor motion than Chest.

Many groups have reported a hysteresis relationship or phase shift between internal (SI) and external (Belly) features.[2,17,18,21,24,31] All 55 session results were visually reviewed, 12 of 13 patients did not show clear hysteresis between SI and PA motions. However, patient LN09 showed hysteresis between SI and PA motions in 5 sessions as displayed in the first row of Fig. 4. Hysteresis exists between PA and Dia_Dome and between SI and Dia_Dome. This type of hysteresis occurred consistently for patient LN09, as seen in Fig. 4, which displays results of 24,705 image frames in 5 sessions.

Hysteresis was not observed for liver patients.[27] Unlike lung cases, liver target SI motions linearly correlate to Dia_Dome with correlation coefficients of 0.97 ± 0.04 for liver tumors located just underneath the diaphragm.[27] The lung tumor of patient LN09 was 86 ± 10 mm superior to the diaphragm, 47 ± 8 mm superior to the diaphragmatic dome, but 158 ± 13 mm posterior to the diaphragmatic dome. Since the lung tumor is far behind the diaphragmatic dome, diaphragmatic motions could not linearly drive the lung tumor motions and resulted in hysteresis between the lung tumor and diaphragmatic motions.

A previous liver patient study found that patient respiratory pattern can change during treatment.[27] As listed in Table E1, among the 6 patients with large motions, in addition to patient LN09, patient LN06 had sessions with weaker SI-Belly correlations (0.67-0.92). This was mainly due to the large spread of Belly positions compared with the relatively small Belly motion ranges (motion standard deviation, 4.1 ± 1.2 mm), as displayed in Fig. E2. In addition, this study was based on motion analyzed from sagittal images. Motion is possible in 3 dimensions. One previous study that focused on patients with liver cancer found that the SI-Belly correlation coefficients had larger dispersion when the sagittal imaging lateral positions moved farther away from body central axis.[27] As illustrated in Fig. E3, similar dependence was observed except for 2 patients (LN01 and LN02) with smaller motion ranges. Multiple orthogonal views and volumetric images must be included to establish more reliable associations.

Different from a previous liver study, large lung tumor SI motions correlated well with both Dia_Dome and Belly.[27] Correlation coefficients were 0.94 ± 0.07 between SI and Dia_Dome and 0.90 ± 0.10 between SI and Belly. Because the SI motion usually dominates lung tumor motions, belly motion may serve as a good surrogate of tumor motion, and one that can be monitored by external surrogates, such as Varian Real-time Position Management, Philips Bellows, or optical surface imaging systems. In addition to MRI, ultrasound may be used to monitor diaphragmatic motion noninvasively. This also suggests that tracking diaphragmatic motions by ultrasound technique could be used to monitor liver or lung tumor motions efficiently.[32]

This study used 177,009 frames of images, which recorded respiratory information, including both internal tumor/organs and external skin motions, lasting for an average of 57 minutes per patient over different days. For the 6 patients with large motions, the average cumulative imaging time was approximately 65 minutes per patient. This is the first report that includes a large quantity of cine images acquired during actual lung cancer treatment for complete treatment courses. This is very different from reports in the literature, which were based on patient data over a short period of time. As such, the correlations we report here are based on realistic data acquired over the full treatment fraction and subject to the changes occurring during the treatment fraction. Our data show that the respiratory patterns can change within a given treatment fraction and are also subject to hysteresis. Deterministic models may not fully describe such behavior and further studies are warranted.[33]

Conclusion

For patients with lung cancer with tumor motion standard deviations of 5 mm or more, lung tumor longitudinal motions are highly correlated with diaphragm and belly motions.

Disclosures

IJC reports institutional, sponsored grants from Varian Medical Systems/Siemens Healthineers and ViewRay Inc, unrelated to this work.

Supplementary materials

Supplementary material associated with this article can be found in the online version at doi:10.1016/j.adro.2023.101271.

References

1. Verellen D, De Ridder M, Linthout N, et al. Innovations in image-guided radiotherapy. *Nat Rev Cancer*. 2007;7:949-960.
2. Keall PJ, Mageras GS, Balter JM, et al. The management of respiratory motion in radiation oncology report of AAPM Task Group 76. *Med Phys*. 2006;33:3874-3900.
3. Jiang SB. Radiotherapy of mobile tumors. *Semin Radiat Oncol*. 2006;16:239-248.
4. Lujan AE, Larsen EW, Balter JM. Ten Haken RK. A method for incorporating organ motion due to breathing into 3D dose calculations. *Med Phys*. 1999;26:715-720.
5. Hu Y, Rankine L, Green OL, et al. Characterization of the onboard imaging unit for the first clinical magnetic resonance image guided radiation therapy system. *Med Phys*. 2015;42:5828-5837.
6. Mutic S, Dempsey JF. The ViewRay system: Magnetic resonance-guided and controlled radiotherapy. *Semin Radiat Oncol*. 2014;24:196-199.
7. Wen N, Kim J, Doemer A, et al. Evaluation of a magnetic resonance guided linear accelerator for stereotactic radiosurgery treatment. *Radiother Oncol*. 2018;127:460-466.
8. Xu Q, Hamilton RJ, Schowengerdt RA, Alexander B, Jiang SB. Lung tumor tracking in fluoroscopic video based on optical flow. *Med Phys*. 2008;35:5351-5359.
9. Boggs DH, Popple R, McDonald A, et al. Electromagnetic transponder based tracking and gating in the radiotherapeutic treatment of thoracic malignancies. *Pract Radiat Oncol*. 2019;9:456-464.
10. Sarkar V, Szegedi M, Paxton A, et al. Preliminary clinical experience with Calypso anchored beacons for tumor tracking in lung SBRT. *Med Phys*. 2020;47:4407-4415.
11. Hoisak JD, Sixel KE, Tirona R, Cheung PC, Pignol JP. Correlation of lung tumor motion with external surrogate indicators of respiration. *Int J Radiat Oncol Biol Phys*. 2004;60:1298-1306.
12. Ahn S, Yi B, Suh Y, et al. A feasibility study on the prediction of tumour location in the lung from skin motion. *Br J Radiol*. 2004;77:588-596.
13. Tsunashima Y, Sakae T, Shioyama Y, et al. Correlation between the respiratory waveform measured using a respiratory sensor and 3D tumor motion in gated radiotherapy. *Int J Radiat Oncol Biol Phys*. 2004;60:951-958.
14. Chen H, Zhong Z, Yang Y, et al. Internal motion estimation by internal-external motion modeling for lung cancer radiotherapy. *Sci Rep*. 2018;8:3677.
15. Koch N, Liu HH, Starkschall G, et al. Evaluation of internal lung motion for respiratory-gated radiotherapy using MRI: Part I—correlating internal lung motion with skin fiducial motion. *Int J Radiat Oncol Biol Phys*. 2004;60:1459-1472.
16. Kanoulas E, Aslam JA, Sharp GC, et al. Derivation of the tumor position from external respiratory surrogates with periodical updating of the internal/external correlation. *Phys Med Biol*. 2007;52:5443-5456.
17. Li G, Wei J, Olek D, et al. Direct comparison of respiration-correlated four-dimensional magnetic resonance imaging reconstructed using concurrent internal navigator and external bellows. *Int J Radiat Oncol Biol Phys*. 2017;97:596-605.
18. Milewski AR, Olek D, Deasy JO, Rimner A, Li G. Enhancement of long-term external-internal correlation by phase-shift detection and correction based on concurrent external bellows and internal navigator signals. *Adv Radiat Oncol*. 2019;4:377-389.
19. ST Antoni, Rinast J, Ma XT, Schupp S, Schlaefer A. Online model checking for monitoring surrogate-based respiratory motion tracking in radiation therapy. *Int J Comput Assist Radiol Surg*. 2016;11:2085-2096.
20. Cho B, Poulsen PR, Keall PJ. Real-time tumor tracking using sequential kV imaging combined with respiratory monitoring: A general framework applicable to commonly used IGRT systems. *Phys Med Biol*. 2010;55:3299-3316.
21. Ionascu D, Jiang SB, Nishioka S, Shirato H, Berbeco RI. Internal-external correlation investigations of respiratory induced motion of lung tumors. *Med Phys*. 2007;34:3893-3903.
22. Mukumoto N, Nakamura M, Sawada A, et al. Accuracy verification of infrared marker-based dynamic tumor-tracking irradiation using the gimbaled x-ray head of the Vero4DRT (MHI-TM2000). *Med Phys*. 2013;40: 041706.
23. Ren Q, Nishioka S, Shirato H, Berbeco R. Adaptive external gating based on the updating method of internal/external correlation and gating window before each beam delivery. *Phys Med Biol*. 2012;57:N145-N157.
24. Wu H, Zhao Q, Berbeco RI, Nishioka S, Shirato H, Jiang SB. Gating based on internal/external signals with dynamic correlation updates. *Phys Med Biol*. 2008;53:7137-7150.
25. Paganelli C, Seregni M, Fattori G, et al. Magnetic resonance imaging-guided versus surrogate-based motion tracking in liver radiation therapy: A prospective comparative study. *Int J Radiat Oncol Biol Phys*. 2015;91:840-848.
26. Yang J, Cai J, Wang HJ, et al. Is diaphragm motion a good surrogate for liver tumor motion? *Int J Radiat Oncol Biol Phys*. 2014;90:952-958.
27. Mao W, Kim J, Chetty IJ. Association between internal organ/liver tumor and external surface motion from cine MR images on an MRI-LINAC. *Front Oncol*. 2022;12: 868076.
28. Bishop CA, Ricotti V, Sinclair CDJ, et al. Semi-automated analysis of diaphragmatic motion with dynamic magnetic resonance imaging in healthy controls and non-ambulant subjects with duchenne muscular dystrophy. *Front Neurol*. 2018;9:9.
29. Ge J, Santanam L, Noel C, Parikh PJ. Planning 4-dimensional computed tomography (4DCT) cannot adequately represent daily intrafractional motion of abdominal tumors. *Int J Radiat Oncol Biol Phys*. 2013;85:999-1005.
30. Steiner E, Shieh CC, Caillet V, et al. Both four-dimensional computed tomography and four-dimensional cone beam computed tomography under-predict lung target motion during radiotherapy. *Radiother Oncol*. 2019;135:65-73.
31. Seppenwoolde Y, Shirato H, Kitamura K, et al. Precise and real-time measurement of 3D tumor motion in lung due to breathing and heartbeat, measured during radiotherapy. *Int J Radiat Oncol Biol Phys*. 2002;53:822-834.
32. Vogel L, Sihono DSK, Weiss C, et al. Intra-breath-hold residual motion of image-guided DIBH liver-SBRT: An estimation by ultrasound-based monitoring correlated with diaphragm position in CBCT. *Radiother Oncol*. 2018;129:441-448.
33. Lujan AE, Balter JM, Ten Haken RK. A method for incorporating organ motion due to breathing into 3D dose calculations in the liver: Sensitivity to variations in motion. *Med Phys*. 2003;30:2643-2649.